Journal of Power Sources 556 (2023) 232375

Contents lists available at ScienceDirect

Journal of Power Sources

journal homepage: www.elsevier.com/locate/jpowsour

Magnetron-sputtered thin-film catalyst with low-Ir-Ru content for water electrolysis: Long-term stability and degradation analysis

Tomáš Hrbek, Peter Kúš *, Yuliia Kosto, Miquel Gamón Rodríguez, Iva Matolínová

Charles University, Faculty of Mathematics and Physics, Department of Surface and Plasma Science, V Holešovičkách 2, 180 00, Prague 8, Czech Republic

HIGHLIGHTS

- We use magnetron sputtered, iridium-ruthenium-based catalyst for OER in PEM-WE.
- Catalyst with low Ir loading (158 μg cm^{-2}). Its composition is 25% Ir, 75% Ru.
- Sputter-etching modification of PEM surface replaces anode supports.
- After 1272 h long operation, we observe 1 A cm^{-2} at 1.641 V.
- Degradation is analyzed daily by PEIS and standard Randles circuit.

GRAPHICAL ABSTRACT

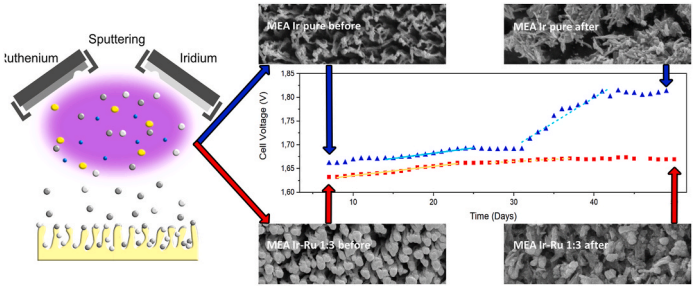

ABSTRACT

Proton Exchange Membrane Water Electrolyzers (PEM-WEs) are entering the phase of commercial mass production. However, the issue of an iridium catalyst for the anode remains. This work presents an iridium-ruthenium-based catalyst (25% Ir = 158 μg cm^{-2}, 75% Ru) prepared as a thin film on the surface-enhanced-anode of PEM-WE via magnetron sputtering. Using a strictly practical single-cell approach, we show its excellent activity – 1 A cm^{-2} at 1.606 V, 80 °C, and stability – 1.3 μV h^{-1} at 1 A cm^{-2} over the period of 500 h. Together with a purely Ir-based catalyst (158 μg cm^{-2}), we subject it to a massive electrochemical and material analysis, showing that the thickness and interconnectivity are essential for the catalyst's stability. Consequently, we believe that magnetron sputtering is currently the most perspective method for preparing low-Ir-loading catalysts. Compared to the nanoparticle approach, it allows the creation of very thin films with unprecedented interconnectivity.

1. Introduction

The production of pure hydrogen by water splitting is a rising phenomenon [1]. Often called green hydrogen, it is a crucial ingredient for achieving the goals of decarbonization outlined by developed countries throughout the world in multiple programs, such as the European Green Deal, the US Green New Deal, etc. [2,3]. The importance of green hydrogen may be found in two main areas: in the industry as a material and in energetics and mobility as an energy vector [4,5]. The former is straightforward – by using green hydrogen, the sector will produce fewer carbon emissions. The latter is more complex, and it revolves around the problematics of renewable sources of electricity – such as solar or wind power plants. Those technologies can potentially replace fossil fuels [6]; however, their intermittent character has to be addressed to assure stable electricity production [6]. Various approaches can guarantee that [7], yet the most perspective one appears to be the hydrogen economy cycle [8]. The main idea is to store the excessive energy in the time of overproduction in the form of molecular hydrogen – chemical energy and then use it for electricity production in times of need. Therefore, the cheap and affordable production of green hydrogen

* Corresponding author.
E-mail address: peter.kus@mff.cuni.cz (P. Kúš).

https://doi.org/10.1016/j.jpowsour.2022.232375
Received 9 August 2022; Received in revised form 20 October 2022; Accepted 6 November 2022
Available online 28 November 2022

by water electrolyzers is crucial.

There are several types of water electrolyzers, which all have their advantages and disadvantages [9]. The most perspective ones are currently Proton Exchange Membrane Water Electrolyzers (PEM-WE), thanks to their high efficiency and ability to be used in real applications in the next few years [10]. Simplified scheme of PEM-WE operation is shown in Fig. S1. The main issue that hinders the possible mass production is the utilization of the noble metal catalysts (Pt, Ir) for the cathodic Hydrogen Evolution Reaction (HER) and anodic Oxygen Evolution Reaction (OER). Especially the four-electron step OER presents a challenge [11]. The sluggish kinetics of OER, high potentials and acidic environment on the anode usually result in the necessity of using significant loadings of Ir (several mg cm^{-2}) to obtain commercially adequate activity and stability. Thus, one of the key research goals is to reduce the amount of iridium on the anode of PEM-WE [10].

Numerous approaches attempt that; we can generally separate them into morphological and material/chemical. The former aims to improve the utilization and dispersion of an employed catalyst to increase its active surface area. Unfortunately, carbon-based materials that demonstrate large surface areas cannot be applied on the anode of PEM-WE due to the high potentials (more than 1.5 V) present therein [10]. High potentials inevitably cause a rapid carbon dissolution into CO_2 [12]. A possible alternative was found in multiple electrochemically resistive supporting materials such as TiO_2 [13], TiC [14], TiN [15], TaC [16], SnO_2 [17], yielding much higher electrochemical resistivity towards the high potentials and significantly improving the active surface area in comparison with unsupported catalysts. The most crucial disadvantage is their limited or non-permanent conductivity, which increases the overall ohmic resistance of the PEM-WE and consequently significantly decreases its performance, especially at higher current densities [18]. An opposite approach may circumvent this issue; instead of additional high-surface support, the surface of the PEM itself may be significantly enlarged by a so-called sputter-etching procedure in a vacuum chamber with a magnetron deposition system during reactive sputtering of CeO_2 [19,20].

Regarding the role of magnetron sputtering, its utilization for the preparation of the low-loading catalysts appears to be a promising alternative to the traditional wet techniques [21–24]. Its significant advantage lies in the deposition of homogeneous, interconnected layers with a better lateral conductivity than in the case of separated nanoparticles with the same loading [25]. Moreover, it is an easily scalable technique currently used in the industry to prepare various coatings and layers [26]. Last but not least, it allows straightforward deposition of bimetallic – or even more complex – layers by co-sputtering without a need to make significant changes in the preparation process.

The second main direction of iridium loading reduction is material/chemical and consists of replacement (complete or partial) of iridium by other material active for OER, which is cheaper. There is extensive research ongoing in the field of entirely non-noble metal-based catalysts, utilizing NiO, CoO, FeO, MnO [27], or various perovskites [28–30]. Unfortunately, the active and stable catalyst that would operate at acidic conditions at high current densities is yet to be found. On the other hand, ruthenium is a noble metal which is much cheaper than iridium and yet even more active toward OER. Its main drawback lies in an extreme electrochemical instability which prevents it from being used as a standalone OER catalyst [31]. Promising results were achieved with Ir–Ru-based catalysts, demonstrating an excellent activity and stability [32–34], especially for very low iridium loading around 20–30% [35,36].

Development of PEM-WE as a whole, its characterization and analysis – including the catalysts – still present a challenge due to the complexity of all involved processes. In particular, there is a significant gap between the conducted research of the catalysts, often done in the half-cell setup, and the real-life applications fittingly called a valley of death [37–39]. The half-cell setup is only helpful in the first material characterization; however, it is not sufficient for definite conclusions about the catalyst usability in real applications [37]. Due to the complex character of the PEM-WE the detailed analysis of the involved processes is complicated, and expensive operando setups are required [40]. On the other hand, electrochemical methods, such as Electrochemical Impedance Spectroscopy (EIS), allow a detailed analysis of the PEM-WE in the operating conditions without any approximations [41]. The principal problem with EIS lies in the complicated and ambiguous analysis of the impedance spectra, relying on Equivalent Electric Circuits (EEC) [42,43]. Therefore, a deeper EIS analysis requires large amounts of data together with a physically meaningful EEC, and a complementary measurement should confirm the results by other techniques [41]. Still, it is a unique technique that allows direct operando insight into the PEM-WE.

This paper presents a complete study of a PEM-WE with a complex, low-iridium-loading catalyst. We combine two subsequently applied approaches using magnetron sputtering - the sputter-etching modification of PEM [20] and a magnetron-sputtered deposition of Ir–Ru-based catalyst with 25% of Ir and 75% of Ru [36]. This catalyst is compared with an Ir one with the same Ir loading during a more than 1000 h lasting degradation procedure of both catalysts in a single-cell PEM-WE – here the Ir–Ru-based catalyst showed excellent activity and stability. Then we present a unique EIS analysis of the degradation of both membranes to find their origin. The conclusions from the EIS analysis are confirmed by results from Scanning Electron Microscopy (SEM), Energy Dispersive X-Ray Spectroscopy (EDX), and X-Ray Photoelectron Spectroscopy (XPS).

2. Experimental

2.1. Preparation of Membrane Electrode Assemblies

Pristine Nafion 212 membranes (50.8 μm thick, Chemours) were used as a solid electrolyte for all samples. The preparation of each Membrane Electrode Assemblie (MEA) was done within a single vacuum entry into a multi-magnetron deposition system. Firstly, the active surface of the membrane was enhanced by the sputter-etching procedure, as described in the work [19]. Secondly, the catalysts layers were deposited: The atmosphere was again pumped down to a base pressure of 5.10^{-5} Pa. Afterwards, the chamber was filled with Ar gas (99.9999%, Linde, 7 sccm), establishing a working pressure of 0.5 Pa. A DC01BP power source (K. J. Lesker) was utilized for the ignition of the plasma discharge over Ir and Ru targets with a diameter of 2" (5.08 cm). Two MEAs with different anode catalysts were prepared. In both cases, the loading of the expensive iridium was held the same, while they differed in the presence of ruthenium. First MEA, referred to as *MEA Ir pure*, contained only a 70 nm thick iridium layer on the anode (Ir loading 158 μg cm^{-2}). The second MEA, henceforth referred to as *MEA Ir–Ru 1:3*, contained 280 nm of a bimetallic Ir–Ru catalyst with atomic composition: 25% of iridium and 75% of ruthenium (Ir loading 158 μg cm^{-2}, Ru loading 256 μg cm^{-2}). The thicknesses were calibrated using the varnish droplet method [44]. The details of the sputtering and catalysts Ir–Ru ratio optimization process are described in Ref. [36], where we studied Ir and Ir–Ru catalytic layers with the same nominal thickness of 50 nm (i.e., different Ir loading) with the focus on their intrinsic activity. After the sputtering, the MEAs were completed by a Liquid Gas Diffusion Layer (LGDL) on the anode and a Gas Diffusion Electrode (GDE) on the cathode side. As the LGDL on the anode, a micro-grained sintered porous Ti (Mott) with a 50 nm protection layer of platinum was employed. As the GDE on the cathode, a commercial platinum catalyst supported by carbon black (Pt 0.5 mg cm^{-2}, FuelCellStore) was used. Moreover, we prepared copies of *MEA Ir pure* and *MEA Ir–Ru 1:3* for results verification.

2.2. MEAs performance in single-cell PEM-WE

The prepared MEAs (for details see Table 1) were pressed between

Table 1
Parameters of the prepared MEAs. $Load_{Ir}$ stands for Ir loading, $Load_{Ru}$ for Ru loading, and thickness for the equivalent thickness of the layer on a plain surface.

Sample	Catalyst anode	LGDL anode	GDE cathode	$Load_{Ir}$ (μg cm^{-2})	$Load_{Ru}$ (μg cm^{-2})	Thickness (nm)
MEA Ir pure	Ir	$Ti_{platinized}$	C + Pt	158	0	70
MEA Ir–Ru 1:3	Ir–Ru	$Ti_{platinized}$	C + Pt	158	256	280

the end-plates with serpentine flow fields (Tandem) made from Ti and C on the anode and cathode sides, respectively, forming a complete PEM-WE with an active surface area of 4.62 cm^2. The electrochemical performance of the MEAs was measured in a dedicated testing station at 80 °C by a SP-150 potentiostat (BioLogic). The reference wire was placed to the cathode; therefore, we present all the voltages in this article versus this reference. The measuring PEM-WE procedure generally consisted of several prolonged, high-impact aging procedures: measurements of IV curves in potentiostatic regime from 1.3 V to 2 V (step 5 mV, duration 10s); applying galvanostatic piles from 0 to 2 A cm^{-2} (step 182 mA cm^{-2}, duration 30 min), and long galvanostatic stability test at 1 A cm^{-2}. Those procedures were then accompanied by electrochemical measurements for MEA characterization – without causing significant degradation - the Cyclic Voltammetry (CV) and Potential Electrochemical Impedance Spectroscopy (PEIS). The CVs were measured in the range of 0.05 V–1.4 V (scanning speed 20 mV s^{-1}) five times. The PEISes were measured at voltages 1.3, 1.35, 1.4, 1.45, 1.5, 1.55, 1.6, 1.7, 1.8, 1.9, 2 V (frequency range 200 kHz–500 mHz, sine amplitude 5 mV). The data from the PEIS measurements were processed by a Python script and Relaxis3 software.

During the first day, only the IV curves were repeatedly measured to break-in the MEA and describe the behavior at the whole range of typical voltages for PEM-WE. From day 2 to day 6, the galvanostatic piles, simulating standard day/night cycles, were applied. From day 7 to day 50, the long galvanostatic aging procedure (more than 1000 h) at 1 A cm^{-2} was used. Ultimately, the IV curves were measured again to compare the original and final states of the investigated MEAs. The operation was terminated sooner if the degradation was too severe. The individual measurement regimes were separated by 2 h at Open Circuit Voltage (OCV); in the case of the galvanostatic piles, the OCV lasted for 12 h to simulate the day/night cycle. Every day, the series of PEISes and CVs were measured. The PEM-WE procedure is summarized in the scheme in Fig. 1. The PEISes and CVs are not included as they would make the scheme less clear and are not causing degradation/aging.

2.3. Physico-chemical characterization of the MEAs

The tested MEAs were always physically characterized in the as-prepared state and after the PEM-WE procedure (post-mortem). The sample morphology was studied by a Scanning Electron Microscope (SEM) Mira III (Tescan), typically with an accelerating voltage of 20 kV in a secondary electron detection mode. A carbon tape had to be used to assure a sufficient electrical conductivity of the sample and thus prevent its charging.

The elemental composition of the catalytical layers was investigated by Energy Dispersive X-ray spectroscopy (EDX). A dedicated XFlash 6/10 EDX detector (Bruker), incorporated into the SEM device, was employed for spectra acquisition. The essential measured elements were iridium and ruthenium; therefore, an accelerating voltage of 20 kV was kept even for EDX measurements to measure the Ir L and Ru M line correctly – those lines were chosen to avoid the issues with overlaying peaks. The elemental composition was calculated by the PB-ZAF approach, by the Quantax software [45]. A large view field of 500 × 500 $μm^2$ was used for all samples to ensure obtained concentrations' integral character. Moreover, we checked several smaller sections with a view field 50 × 50 $μm^2$ to confirm the elemental homogeneity of the samples. For the data interpretation, we must consider that the information depth of EDX is in order of μm; therefore, from the point of view of the investigated layers with thicknesses not larger than 300 nm, it is a bulk-sensitive method.

The surface elemental and chemical composition was studied by X-ray Photoelectron Spectroscopy (XPS) in an EnviroESCA device (SPECS). We used a monochromatized $K_α$ Al X-ray source (1486.71 eV) for X-ray generation. The signal detection was done by a Phoibos 150 NAP 1D-DLD (SPECS) hemispherical energy analyzer in FAT (Fixed Analyzer Transmission) mode. This powerful setup allows picking exactly the desired area for XPS analysis by a laser pointer. Thanks to the compatibility of the sample holders for SEM Mira III and EnviroESCA, we were able to measure the same samples at the same spots for all the MEAs (SEM, EDX, and XPS as well). The subject of interest was the core levels: Ir 4f, Ru 3d, C 1s and O 1s. The number of scans for each element was adjusted to obtain a sufficient signal/noise ratio. The measured spectra were compensated for charging by leveling Fermi edges to 0 eV binding energy and fitted utilizing KolXPD software. Shirley's model was used for the peaks background subtraction [46]. The peaks themselves were fitted either by symmetric Voigt profiles or asymmetric Doniach-Sunjic type of peaks convoluted with Gaussians – the peak types were chosen based on the literature for each element, as well as the peak splitting and ratios for doublets [47–49]. The concentrations of iridium and ruthenium were calculated by the sensitivity factors approximation [50].

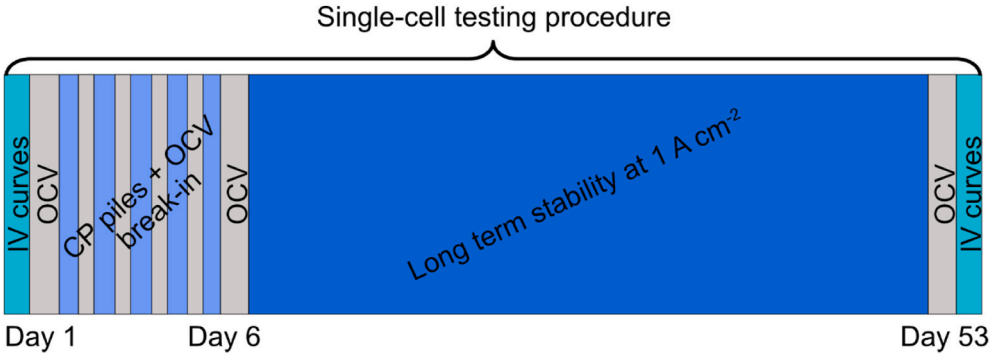

Fig. 1. The scheme of the utilized testing procedure for single-cell PEM-WE. Cyan stands for measurements of IV curves, light blue for galvanostatic piles procedure, dark blue for long-term stability at 1 A cm^{-2}, and grey for Open Circuit Voltage (OCV). PEISes and CVs were measured each day and are not depicted in the scheme. (For interpretation of the references to colour in this figure legend, the reader is referred to the Web version of this article.)

3. Results and discussion

3.1. Activity evaluation

The PEM-WE procedure described in the Experimental section was applied for both MEAs. The IV curves at the end of the first and last day are in Fig. 2. Note that the data presented in this article are without any ohmic resistance correction (IR) as it is an operation that does not correspond to the actual applications of the PEM-WE [37]. Firstly, we can see that while *MEA Ir–Ru 1:3* degrades only slightly in the span of 53 days (1272 h), *MEA Ir pure* degrades significantly already in 50 days; therefore, the measurement was stopped sooner due to the massive degradation. Uncovering this effect will be done later. In terms of MEA activity, according to our previous studies [36], the Ir–Ru 1:3 catalyst shows better activity than pure Ir one, the primary purpose of which is to be a reference for a solely Ir-based catalyst. In the beginning, MEA Ir–Ru 1:3 produces 1 A cm^{-2} at 1.606 V, 2 A cm^{-2} at 1.726 V, and 4 A cm^{-2} at 1.935 V, thus catching up on high Ir-loading catalysts [17,51–54] and surpassing multiple catalysts with low Ir content reported before [52,55–57]. From the point of view of our motivation: removing Ir as the limiting factor for massive decarbonization by PEM-WE, we obtain the Ir-specific power density of 0.033 g kW^{-1} at 1.79 V cell voltage. The study [47] analyzes that 0.01 g kW^{-1} (calculated at 1.79 V) should be sufficient to fully replace all fossil fuels with green hydrogen. Considering that high loading PEM-WE typically has 0.5 g kW^{-1}, we see that we are getting closer to the target. Moreover, we should emphasize that, in reality, we can operate the PEM-WE at higher voltages than 1.79 V. Furthermore, it is not expected that all the fossil fuels have to be replaced solely by hydrogen – other technologies, such as batteries, will undoubtedly take part.

3.2. Pile procedure and long stability test

Now, we will focus on the stability, which is often the crux of low Ir-loading catalysts for PEM-WE [10]. During applying the galvanostatic piles up to 2 A cm^{-2}, the MEA performance showed small fluctuations (not shown), suggesting prolonged breaking-in Ref. [58]. However, it completely stabilized after day 6, as presented in Fig. 3. *MEA Ir–Ru 1:3* still demonstrates lower cell voltage (i.e., better performance) than *MEA Ir pure* – 1.726 versus 1.760 V at 2 A cm^{-2}. A fact worth noticing is that the *MEA Ir–Ru 1:3* with a thicker layer of bimetallic catalyst needed

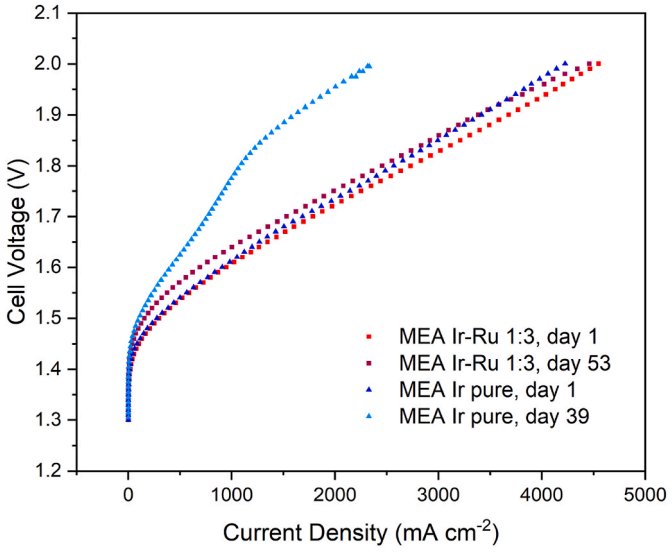

Fig. 2. IV curves measured at the 1st and 53rd day for MEA Ir–Ru 1:3 and at the 1st and 50th day for MEA Ir pure. While the former shows only minimal degradation, the latter degraded significantly in a shorter time.

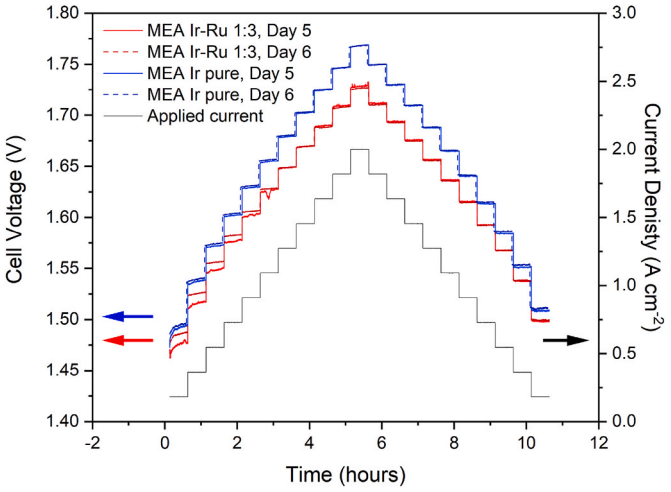

Fig. 3. The stabilized curves after the five-day break-in procedure with the profile of applied current density.

more time to stabilize appropriately. Still, we present the curves from the same day for both MEAs to simplify the interpretation.

The galvanostatic procedure was followed by the long-term aging stability measurement at 1 A cm^{-2}. The resulting cell voltages (Fig. 4) were taken as an average of 20 points at the end of each day just before the measurements of PEIS. Error bars are negligible compared to the size of the points – there were no abrupt changes in the cell voltage.

Here, we emphasize two main types of degradation: reversible and irreversible [59]. The reversible degradation can be easily mitigated by a brief shutdown of the PEM-WE. At the same time, the irreversible one does not change and is connected directly to the structural and chemical changes in PEM-WE. Therefore, degradation reporting is often done after a shutdown, inevitably improving degradation rates and performances [60]. Unfortunately, at the same time, it compromises possible comparisons between published data as the performance maybe eventually more dependent on the interruption procedure than on the catalyst itself [61]. Since the reversible degradation has been reported as exponential at the beginning and linear later [62], we suggest the opposite approach: to document the performance after a long time of reversible degradation when it has a lower impact on the performance. This approach again mirrors the natural conditions of the PEM-WE operation; moreover, it ensures that the investigated sample did not get any advantage, which might compromise the interpretation. Therefore, the long galvanostatic stability tests at 1 A cm^{-2} will contain both reversible and irreversible degradation. Finally, we can obtain the overall irreversible degradation by comparing the IV curves at beginning of the PEM-WE procedure and its end. The 12 h long OCV shutdown between the procedures will mitigate the reversible degradation. We can also compare the reversible and irreversible degradation effects by setting side-by-side the voltages at 1 A cm^{-2} from Fig. 2, day 50 (*MEA Ir pure*), 53 (*MEA Ir–Ru 1:3*), and Fig. 4, day 49 (*MEA Ir pure*), 50 (*MEA Ir–Ru 1:3*). The most straightforward is a detailed analysis of the galvanostatic degradation curve in Fig. 4. We can distinguish two main regimes: a linear growth of the cell voltage and no visible changes in potential. A corresponding linear function fitted well in those regions (see Fig. 4). The fits parameters are in Table S1 of the Supplementary Information (SI) together with the low mean-square errors confirming linear behavior. Moreover, the linearity of the degradation was observed in multiple previous studies [59,62]. However, the linear regions are not continuous in our case – large parts of zero degradation intermit them; therefore, we expect that the origin of the degradation is a complicated process.

Total degradation rates for the 1 A cm^{-2} stability test and the partial degradation rates between the days 7–23 and 23–50 calculated from

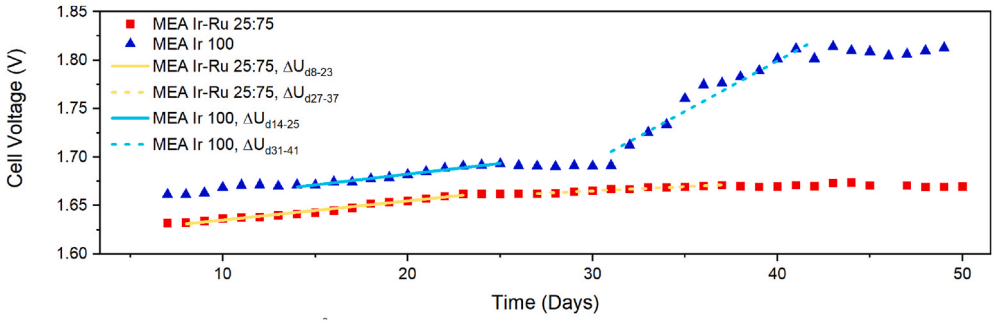

Fig. 4. Cell voltage at 1 A cm^{-2} and its evolution during the long-term stability with the fitted region of linear degradation.

data in Fig. 4 are presented in Table 2. It is obvious that the presence of Ru in *MEA Ir–Ru 1:3* leads to significantly better stability than in the case of pure Ir. *MEA Ir pure* shows massive degradation after day 31. This phenomenon will be investigated later. Now we focus on the stability of *MEA Ir–Ru 1:3*. The degradation rate between days 7 and 23 is 82.4 μV h^{-1}, even slightly higher than for *MEA Ir pure*. Still, it is a good value compared to other low Ir-loading PEM-WEs [55]. However, from day 23, the performance stabilized significantly, resulting in a degradation rate of only 1.3 μV h^{-1}. There were no signs of more pronounced degradation; on the contrary, the performance got stable from day 40 to day 50. The value of 1.3 μV h^{-1}surpassed the number recently reported on catalysts with similarly low Ir-loading [56,63] and is lower or equal to those obtained from systems with high iridium loading [59,64]. Similar values were reported in studies [65,66]; however, with a 2–2.5 times higher Ir loading and worse activity (i.e., higher cell voltage at 1 A cm^{-2}). The comprehensive list of recently published low-Ir-loading catalysts and their performance is in Table 3.

To summarize above results, *MEA Ir–Ru 1:3* demonstrates an unparalleled activity and stability with a loading of 158 μg cm^{-2} of Ir and an easily scalable preparation method. The remaining question is what is behind those parameters, and why is *MEA Ir pure*, with the same Ir loading significantly worse? To understand that, we need to analyze the degradation process more thoroughly.

3.3. Electrochemical analysis of degradation – DC measurement

To explain the high level of degradation of *MEA Ir pure* compared to *MEA Ir–Ru 1:3*, firstly, we will use electrochemical data to provide operando information from the whole measurement. Later, we will confront the electrochemical results with data obtained by other applied methods.

Cyclic Voltammetry (CV) uncovers further information about the electrochemical system. It generally allows studying oxidative and redox behavior over a wide potential range [70]. Unfortunately, the broad scale of processes and high complexity of the PEM-WE complicate the analysis of CVs. Moreover, the presence of oxygen on the anode and hydrogen on the cathode may change the potentials of the occurring reaction, therefore leading to distorted results [71]. We show the CVs from both MEAs (days 2 and 48) in Fig. S2 of the SI; however, we do not do any quantitative analysis. The most important qualitative observations from the CVs are, based on [72], that in the case of MEA Ir, in the beginning, we see only a very sharp OER peak with no further significant reactions, while after the stability, we also see a broad shoulder before OER onset, associated with the further oxidation of Ir^{3+}. Based on this, we suggest that *MEA Ir* is purely metallic at the beginning; however, with time the Ir oxidise. Using the same logic for *MEA Ir–Ru 1:3*, we see the broad peak of Ru^{4+} species oxidation both before and after the stability. We conclude that most likely Ru was oxidized from the very beginning. This corresponds very well with the higher reactivity of Ru, compared to Ir. Thus, only the catalyst in *MEA Ir pure* was completely metallic at the beginning of the tests [66,72].

Table 2
Directly calculated rates of total voltage increment at 1 A cm^{-2} before day 23 (ΔU_{d7-23}), and between days 23 and 50 (ΔU_{d23-50}), and the overall (ΔU_{d7-50}) from the cell voltage evolution curves presented in Fig. 4 for both studied MEAs.

Sample	ΔU_{d7-23} (μV h^{-1})	ΔU_{d23-50} (μV h^{-1})	ΔU_{d7-50} (μV h^{-1})
MEA Ir–Ru 1:3	82.4	1.3	36.9
MEA Ir 100	75.6	282.8	153.7

Table 3
The stability performance of a low-Ir-loading anode catalyst for PEM-WE from the recent three years.

Author	System	Ir loading (μg cm^{-2})	Degradation rate (μV h^{-1})	Note
Haoran Yu [63]	IrOx + Nafion	80	400	1.92 V @ 1.8 A cm^{-2} after 1000 h
Devashish Kulkarni [67]	IrOx + Nafion, printed	160	63000	2.5 V @ 1.5 A cm^{-2} after 90 h
Ahyoun Lim [68]	ED Pt@IrO_2	160	155	1.53 V @ 0.4 A cm^{-2} after 220 h
Friedemann Hegge [55]	IrO_x hybrid layer	200	200	1.75 V @ 1 A cm^{-2} after 150 h
Maximilian Möckl [69]	Hydrous IrO_x catalyst (P2X)	250	56	1.79 V @ 1 A cm^{-2} after 890 h

3.4. Electrochemical analysis of degradation – AC impedance measurement

PEIS was used for deeper electrochemical analysis in operando. Randles EEC describes the behavior of PEM-WE [41,73]; therefore, we use it for fitting. However, since the cathode impedance is low, localized in the high-frequency region, and constant, it was neglected, and only the anodic semicircle was fitted. Thus, the complete Randles circuit shown in Fig. 5 a) for whole PEM-WE was simplified to the scheme in Fig. 5 b). Here, R_1 is the overall ohmic resistance of the cell, which is in series with a parallel combination of anodic charge transfer resistance R_2 and constant phase element P.

The obtained evolution of the ohmic resistance with error bars is in Fig. 6 a) and b) for *MEA Ir–Ru 1:3* and *MEA Ir pure*, respectively. The graphs have two dimensions – the dependency of R_1 on time and cell voltage. The time dependency shows specific changes in ohmic resistance, which we connect to the deterioration of the catalyst and cell components (a growing trend) [59] and the membrane thinning (decreasing trend) [56,74]. In the case of *MEA Ir–Ru 1:3,* changes are not abrupt and relatively insignificant as the ohmic resistance returns almost back to the initial value after 1000 h. In the case of *MEA Ir pure*, there is a

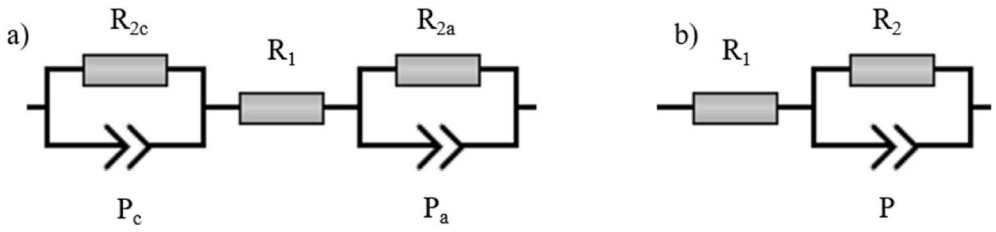

Fig. 5. Equivalent electrical circuits used for fitting: a) Complete Randles circuit, b) Simplified Randles circuit with neglected cathodic reaction. R_1 is ohmic resistance, R_2 is charge transfer resistance, and P is constant phase element, c means the cathode, a the anode.

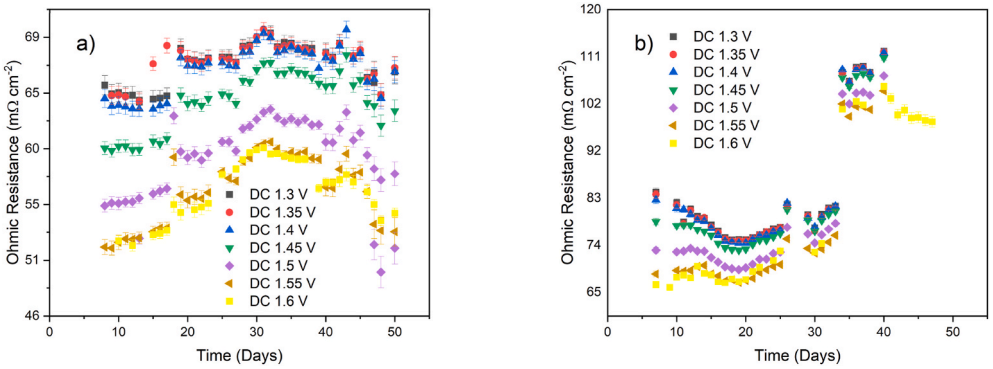

Fig. 6. Evolution of ohmic resistance at different voltages with error bars of the fit a) for MEA Ir–Ru 1:3, b) for MEA Ir pure.

significant jump in ohmic resistance between the days 33 and 34 – therefore, after the beginning of degradation (see Fig. 4). We can use the maximal changes of R_1 to evaluate the maximal possible effect of ohmic resistance on the degradation at 1 A cm^{-2}. Using the values of R_1 at 1.6 V and the Ohm's low, we get roughly 6 mV for *MEA Ir–Ru 1:3* and 34 mV for *MEA Ir pure*. That is in order of magnitude lower than the total degradation of both MEAs during the PEM-WE procedure (see Table 2); therefore, the leading cause of degradation is not increment in ohmic resistance.

In Fig. 6 a) and b) one can see the decreasing ohmic resistance R_1 with growing cell voltage. We do not expect that this effect is directly connected to the cell degradation. A similar effect has been observed in other studies [74,75], yet on entirely different scales, e.g. in Ref. [75] no changes were observed in 1 A cm^{-2} and a 15% decrease in 5 A cm^{-2}, while we observed 20% decrease already at 0.5 A cm^{-2}. One possible explanation is the enhanced PEM conductivity due to the locally increased temperature [75]. However, that would suggest that we should observe a further decrease of R_1 with growing current density, which is not the case – the reduction of R_1 in our case stopped above 1.55 V. Moreover, if we fit the main trend of R_1 on the cell voltage (see an example in Fig. S3 of the SI) by a linear function (the time evolution in Fig. S4), we can see that the slope is approximately −15 mΩ V^{-1} and -10 mΩ V^{-1} for *MEA Ir–Ru 1:3* and *MEA Ir pure*, respectively. Therefore, if it continues this trend, it will lead to zero or negative ohmic resistance at high voltages, which is not observed (and not possible). Therefore, we expect some other ongoing mechanism. We suggest that it might be due to the structure of the sputter-etched membrane (Fig. S5 of the SI), where the individual fibers could be heated much faster than the rest of the PEM, which might cause the observed behavior. However, uncovering this effect is most likely not crucial for the main subject of this article – the degradation; therefore, we will focus on its complete elucidation in our subsequent works.

The charge transfer resistance R_2 (Fig. 5b)) manifests the corresponding activation losses; therefore, we can directly connect it with the activity of the catalyst [41,42]. Qualitatively, it applies that lower charge transfer resistance means higher activity. The charge transfer resistances for voltages above 1.45 V are in Figures S5 a) and b) of the SI for *MEA Ir–Ru 1:3* and *MEA Ir pure*, respectively. We do not present all results due to the vastly differing values at different voltages; the trend is always the same – increasing with time and decreasing with growing voltage.

The charge transfer resistance can also serve for quantitative analysis [76]. Multiple studies determined the Tafel slope from the dependency of the charge transfer resistance on overpotential [77–79]. The dependence is logarithmized and fitted by a linear function. The fitted slope then corresponds to the Tafel slope. The exchange current density can be associated with the intersection of the linear process with the axis Y [80]. Unfortunately, certain doubts are in place about applicability in PEM-WE due to the other currents that can occur at lower voltages due to the cross-over effect, etc. [81]. Nevertheless, we calculate both the Tafel slope evolution presented in Fig. 7 and the exchange current

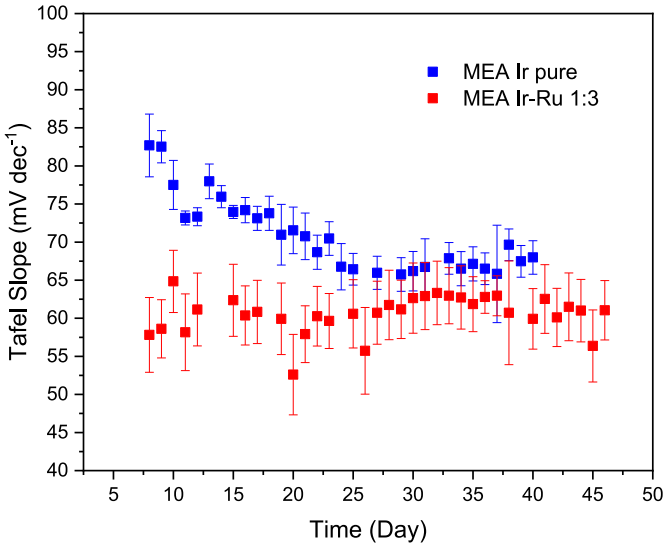

Fig. 7. The evolution of Tafel slope for MEA Ir pure and MEA Ir–Ru 1:3 with error bars.

density in Fig. S7 of the SI. The latter approach is advantageous in PEM-WE as it removes any effects of ohmic resistance R_1 on the real potential of the catalyst. On day 8 the Tafel slopes were 57.8 mV dec^{-1} and 82.7 mV dec^{-1} for *MEA Ir–Ru 1:3* and *MEA Ir pure*, respectively. We can compare it with the values on day 40–59.9 mV dec^{-1} for *MEA Ir–Ru 1:3* and 68.0 mV dec^{-1} for *MEA Ir pure*. Those final values of Tafel slopes correspond well to those reported in our previous study in the half-cell (64.7 mV dec^{-1} *for Ir–Ru 1:3*, 70.9 mV dec^{-1} for *Ir pure*, both after the PEM-WE measurements) [36]. The lower values in our case are caused by the ohmic drop compensation, which is automatic for the method utilizing PEIS. Those values are well in the accepted ranges of Tafel slopes for OER [82,83]. The exchange current densities presented in Fig. S7 correspond in order of magnitude to those reported for the anode of PEM-WE [84], the values for *MEA Ir–Ru 1:3* are slightly higher than for *MEA Ir-pure*. However, we still believe that due to the possible cross-over effects it is not the most reliable merit for evaluating the PEM-WE performance, and therefore we do not comment on them any further.

From Fig. 8 and S6, we can conclude that the loss of catalyst activity is not the cause of the degradation of *MEA Ir pure*. There are no abrupt changes in Tafel slopes or exchange currents associated with the degradation around day 31 for *MEA Ir pure* (Fig. 4). The Tafel slope changes only slightly (*MEA Ir–Ru 1:3*) or even decreases (*MEA Ir pure*), the exchange current densities decrease for both MEAs; however, in a very similar manner.

Based on the above results, we excluded both R_1 and R_2 as the origin of the MEA Ir pure degradation. Thus, the remaining unexplored circuit element from Fig. 5 b) is the constant phase element P, used to model complicated, real processes with several different time constants. They typically originate in the surface roughness, limited dimension, material inhomogeneity, potential inhomogeneity, etc. [85–87]. It can be described by two parameters: Q and α, which are obtained from the fitting procedure [88]. We present Q and α in Figures S7 a), S8 a) for MEA Ir–Ru 1:3 and for MEA Ir pure in Figures S7 b), S8 b) of the SI. However, those values do not have a direct physical meaning. For our case, it is possible to use them to calculate the real capacitance C using the formula [89]:

$$C = \frac{1}{Q(\omega_m)^{1-\alpha}}$$

where ω_m is the frequency that corresponds to the maximum imaginary resistance of the constant phase element semicircle. We use a dedicated Python script to obtain ω_m. Subsequently, the values of real capacitance were calculated and presented in Fig. 8 a) for *MEA Ir–Ru 1:3* and Fig. 8 b) for *MEA Ir pure*, respectively. We present only the curves above 1.45 V for clarity, as they are not affected by the significant dependence of the double-layer capacitance on voltage around zero charge potential [90]. Those effects made the graph incomprehensible for lower voltages. In Fig. 8 a) and b), it can be observed that before the massive degradation of *MEA Ir pure*, both MEAs had similar capacitance around 25 mF cm^{-2}, a typical value for PEM technologies [91]. The capacitance of *MEA Ir–Ru 1:3* is almost stable throughout the whole PEM-WE procedure, while the capacitance of *MEA Ir pure* significantly decreases (from 25 mF cm^{-2} to 17 mF cm^{-2}) between the days 20–31, immediately followed by the massive degradation as presented in Fig. 4. Therefore, it does not accompany the performance deterioration – it precedes it. We can explain this taking a deeper look at the character of observed double layer capacitance in PEM-WE. As illustrated in Refs. [91,92], it is located on the interface between the PEM and catalyst. Therefore, its decrement means that the contact between the catalyst and PEM reduces while the PEM ion conductivity may still be sufficient for the catalyst to function properly (triple-phase boundary condition [14]). The changes in the layer homogeneity will eventually disrupt the necessary lateral conductivity of the layer, crucial for the PEM-WE performance [23,93]. Therefore, our hypothesis based on the PEIS analysis is that the extensive degradation of *MEA Ir pure* was caused by the smaller layer thickness, which is prone to layer disintegration and thus disconnection. The second reason is its lower activity which means it operated at higher, more degrading voltages than MEA Ir–Ru 1:3. However, this hypothesis must be confirmed by other methods of characterization.

3.5. Physico-chemical characterization of the MEAs

So far, we have investigated the MEAs performance and degradation only through electrochemical methods. Now we focus on the detail characterization of both MEAs by other methods to confirm our conclusions.

Firstly, we are interested in the elemental composition of *MEA Ir–Ru 1:3*. The bulk (EDX) and surface (XPS) atomic concentrations of Ir and Ru in *MEA Ir–Ru 1:3* before and after the testing in PEM-WE are in Table 4. Note that the X-Ray Diffraction (XRD) and Transmission Electron Microscopy (TEM) data are in our previous publication [36]. The catalytic layer in the as-prepared state can be considered homogenous as the composition is the same in bulk and on the surface, concerning different methods and errors of estimation. As a result of the 1272 h of operation in PEM-WE, the relative amount of ruthenium decreased both in bulk (less) and on the surface (more); however, it stayed undoubtedly abundant in the catalytic layer. That confirms that an iridium-ruthenium-based catalyst is a suitable and stable option for PEM-WE.

Table 4
Difference in the elemental composition of the catalyst in MEA Ir–Ru 1:3 before and after the PEM-WE procedure.

	XPS results		EDX results	
Sample	Ir [at. %]	Ru [at. %]	Ir [at. %]	Ru [at. %]
MEA Ir–Ru 1:3 before	24.3	75.7	25.2	74.8
MEA Ir–Ru 1:3 after	69.3	30.7	65.7	34.3

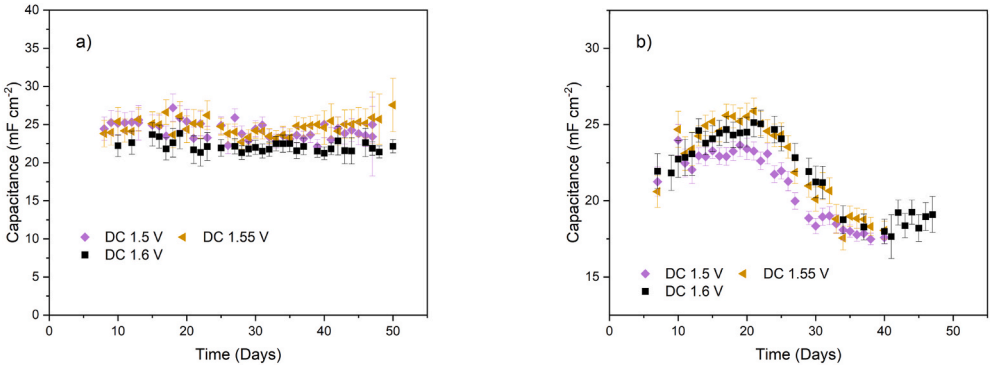

Fig. 8. The evolution of the calculated capacitance per area for voltages 1.5 V, 1.55 V, 1.6 V a) of MEA Ir–Ru 1:3, b) of MEA Ir pure.

Moreover, it strongly supports the hypothesis about the iridium-ruthenium stabilization effect from our previous publications. So far, it was reported in several half-cell studies or shorter single-cell operations [33,43,94]; however, not on this scale. Incomparably, a pure Ru-based catalyst degraded entirely in order of minutes [36].

Secondly, we focus on a deeper analysis of the surface chemical state of the given elements by XPS. We use the binding energies format. XPS Ir 4f and Ru 3d core-level spectra were fitted in accordance with studies [95,96] and our previous work [36]. We used asymmetric line shapes instead of several satellite peaks (for details see Experimental). All binding energies are summarized in Table S3 in the SI.

The Ir 4f spectra of both MEAs as prepared (see Fig. S10) establish the dominance of the Ir metallic state (60.9 eV) and a small amount of IrO_2 (61.8 eV) [96,97], thus confirming the high purity of magnetron sputtered layers. The Ir 4f spectra after the PEM-WE procedure are in Fig. 9. In the case of *MEA Ir pure,* the metallic iridium state disappeared utterly; only IrO_2 (61.8 eV) and $Ir(OH)_x$ (62.8 eV) [96] are present. On the other hand, Ir 4f spectra of *MEA Ir–Ru 1:3* also contain metallic Ir states (the shoulder in the Ir 4f spectra at the binding energy 60.9 eV). The observed metallic state in the more stable *MEA Ir–Ru 1:3* may shed more light on the stabilization effect of the Ir–Ru catalyst – the Ir–Ir metal-like interaction has been reported as more durable than the oxide binding states [98].

The normalized Ru 3d spectra for *MEA Ir–Ru 1:3* before and after the PEM-WE procedure are presented in Fig. 10. The as-prepared layer contains, among the metallic ruthenium (280.1 eV) [99], considerable amounts of a ruthenium oxide. In comparison, Ir is present only in metallic state (Fig. S10). This reflects the higher reactivity of ruthenium, in this case with the atmospheric oxygen. Ru becomes entirely oxidized after the PEM-WE procedure. The dominant oxide is RuO_2 (280.9 eV) [99] which is associated with a superior OER activity [34]. Smaller amounts of other states $Ru(OH)_x$ (282.2 eV) [99] and RuO_4 (283.4 eV) [33] are presented as well, as is typical for Ir–Ru-based systems [33].

On the as-prepared layers, we observe only a C 1s peak at 283.9 eV assigned to carbon impurities [100]. On the spectra from both MEAs after electrochemistry, a new carbon state at 291.4–291.5 eV appears. We associate this peak with the CF_2 bond in Nafion [101], suggesting that the PEM membrane is partially exposed from the catalytic layer. Fig. 10 and S10 show that the ratio between the impurity carbon and CF_2 carbon is 4.2 in *MEA Ir–Ru 1:3* while 0.68 in *MEA Ir pure*, both after the PEM-WE procedure. That confirms that the coverage and uniformity of the catalytic layer at *MEA Ir pure* was compromised – the PEM underneath is significantly more uncovered.

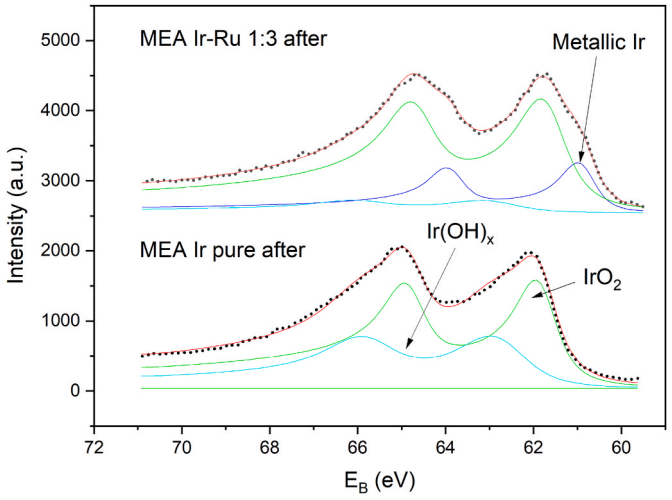

Fig. 9. XPS Ir 4f spectra after PEM-WE procedure. Normalized by the peak height. Color code: black dots – experimental points, red line – sum of the fits; fitted states: blue – Ir metallic, green – IrO_2, cyan – $Ir(OH)_x$. (For interpretation of the references to colour in this figure legend, the reader is referred to the Web version of this article.)

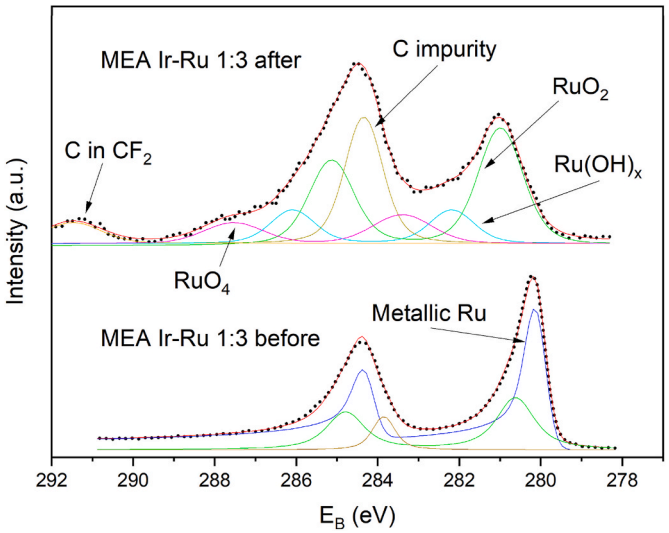

Fig. 10. XPS Ru 3d and C 1s spectra after the PEM-WE procedure. Normalized by the peak height. Color code: black dots – experimental points, red line – sum of the fits; fitted states: blue – Ru metallic, green – RuO_2, cyan – $Ru(OH)_x$, magenta – RuO_4, dark brown – carbon impurity, light brown – carbon in CF_2, Nafion. (For interpretation of the references to colour in this figure legend, the reader is referred to the Web version of this article.)

The presented electrochemical and material information confirm our hypothesis – both Ir and Ir–Ru 1:3 catalysts are stable. The massive degradation of MEA Ir pure was likely caused by the very thin active layer, which lost its lateral conductivity and interconnectivity. To prove it, we follow our analysis by an SEM morphology imaging. Obtained SEM images with a 10 μm × 10 μm view field are in Fig. 11. The morphologies of *MEA Ir–Ru 1:3* and *MEA Ir pure* differ already in the prepared state, reflecting the thicker catalyst layer of *MEA Ir–Ru 1:3*. The fibers of *MEA Ir–Ru 1:3* of the sputter-etched PEM were turned into columnar structures, while the fibers of MEA Ir pure keep the original shape as presented in Fig. S5 in the SI. The crucial are the images after the PEM-WE procedure: the observed *MEA Ir–Ru 1:3* keeps an interconnected catalytical layer, while the layer of *MEA Ir pure* is damaged, cracked, and separated with detached islands of the catalyst visible. Therefore, Fig. 11 completes the picture of *MEA Ir pure* and the origin of its degradation. More detailed SEM images of the layers on the sputter-etched PEM are in Fig. S12, where we show morphology with a view field of 1 μm × 1 μm.

A valid argument is that the cracks on *MEA Ir pure* might be produced solely by the pressure and the expansion of the PEM due to the water exposure, not by the electrochemical degradation. However, as seen in Fig. S13, the pressed, wetted, and heated layer which did not perform under potential does not demonstrate the cracks and damage observed in Fig. 11. Therefore, the SEM images from Fig. 11, S12, and S13 confirm our hypothesis about *MEA Ir pure* degradation. Moreover, we have prepared replicas of both *MEA Ir–Ru 1:3* and *MEA Ir pure* and tested them in a second testing station. The used potentiostat did not allow the PEIS measurements; however, we measured the same galvanostatic stability and observed the same type of degradation – a massive one after a few weeks for *MEA Ir pure* and a slow one which eventually stabilized for *MEA Ir–Ru 1:3*. Therefore, we confirmed the reproducibility of the presented results.

4. Conclusion

In this work, we present a iridium-ruthenium-based (25% Ir, 75% Ru) catalyst prepared by magnetron-sputtering for the anode of the

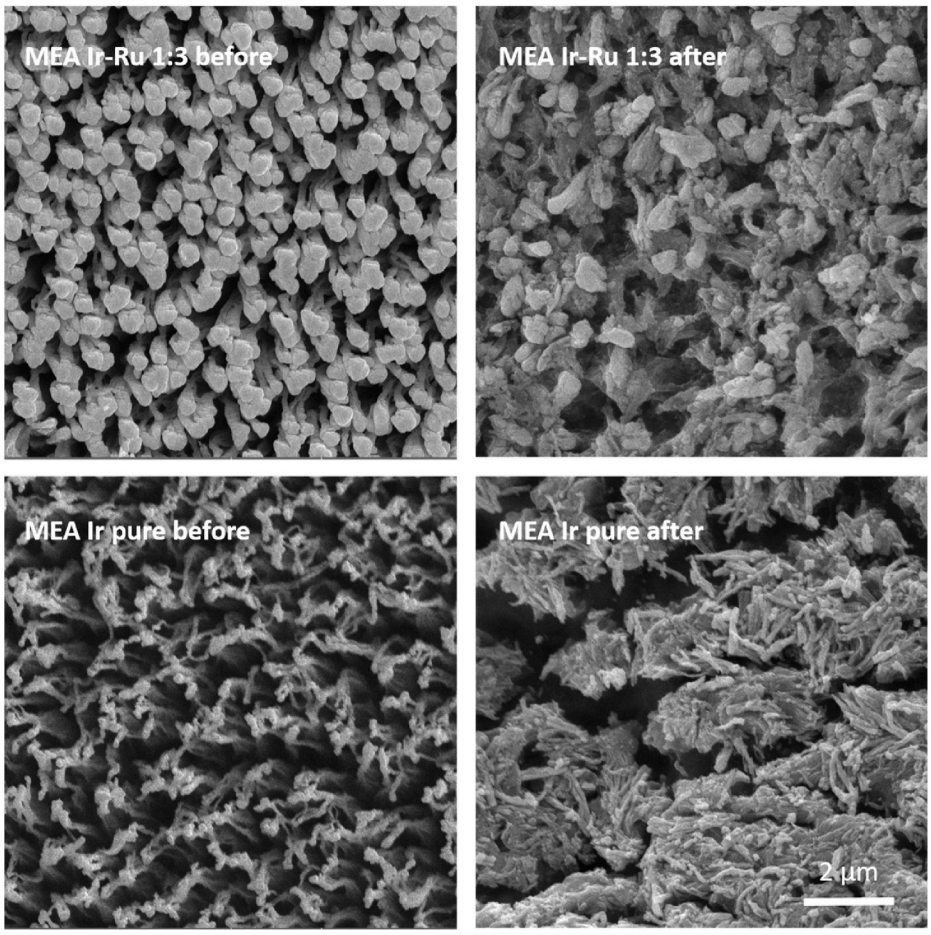

Fig. 11. SEM images of the MEA Ir–Ru 1:3 and MEA Ir pure measured before and after the PEM-WE procedure in the single-cell testing station. The view field is 10 µm × 10 µm for all images.

Proton Exchange Membrane Water Electrolyzer (PEM-WE). We replace the standard catalysts supports as TiO_2, TiN, or TiC with a novel, sputter-etching approach that increases the membrane's active surface area. The Ir–Ru catalyst is utilized in *MEA Ir–Ru 1:3*; the same Ir loading is then used in the *MEA Ir pure*, demonstrating the effect of ruthenium and a thicker catalyst layer. After the PEM-WE procedure with a total length of 1272 h, *MEA Ir pure* shows massive degradation, while *MEA Ir–Ru 1:3* degrades only moderately. We found that the Ir–Ru 1:3 catalyst shows superior electrochemical activity, approaching the ultimate goals of the PEM-WE's anode catalyst research – being able to replace fossil fuels with green hydrogen. Followingly, we uncover the origin of the *MEA Ir pure* degradation, its thinness. The inevitable electrochemical changes bonded to the catalyst operation led to the loss of the interconnectivity of the catalyst, finally causing the failure of the MEA Ir pure.

To conclude, the magnetron-sputtered thin-film catalysts can solve the iridium issue on the anode of PEM-WE as they allow decreasing the Ir loading without the loss of the catalyst interconnectivity and lateral conductivity, which is problematics for the nanoparticle-based catalysts – provided it is complemented by another element to ensure sufficient thickness while not increasing the noble metal content. We consider this the most significant advantage of the magnetron-sputtering approach, together with its simple industrial scalability.

CRediT authorship contribution statement

Tomáš Hrbek: Conceptualization, Methodology, Investigation, Writing – original draft. **Peter Kúš:** Supervision, Investigation, Validation, Writing – review & editing. **Yuliia Kosto:** Investigation. **Miquel Gamón Rodríguez:** Investigation. **Iva Matolínová:** Funding acquisition, Project administration.

Declaration of competing interest

The authors declare that they have no known competing financial interests or personal relationships that could have appeared to influence the work reported in this paper.

Data availability

Data will be made available on request.

Acknowledgment

This work was financially supported by grant No. CZ.02.1.01/0.0/0.0/16_025/0007414, OP VVV project PaC NG. TH acknowledges financial support from the Grant Agency of Charles University in Prague (GAUK No. 336922).

Appendix A. Supplementary data

Supplementary data to this article can be found online at https://doi.org/10.1016/j.jpowsour.2022.232375.

References

[1] A.M. Oliveira, R.R. Beswick, Y. Yan, ScienceDirect A green hydrogen economy for a renewable energy society, Curr Opin Chem Eng 33 (2021), 100701, https://doi.org/10.1016/j.coche.2021.100701.

[2] European Commission, The European green deal, European Commission 53 (2019) 24, https://doi.org/10.1017/CBO9781107415324.004.

[3] R. Galvin, N. Healy, Energy Research & Social Science the Green New Deal in the United States : what it Is and How to Pay for it, 2020, p. 67, https://doi.org/10.1016/j.erss.2020.101529.

[4] R.A.M. Ramachandran, AN OVERVIEW OF INDUSTRIAL USES OF HYDROGEN 23 (1998) 593–598.

[5] Z. Abdin, A. Zafaranloo, A. Rafiee, W. Mérida, W. Lipiński, K.R. Khalilpour, Hydrogen as an energy vector, Renew. Sustain. Energy Rev. 120 (2020), https://doi.org/10.1016/j.rser.2019.109620.

[6] V. Konovalov, O. Pogharnitskaya, A. Rostovshchikova, I. Matveenko, Potential of renewable and alternative energy sources, IOP Conf. Ser. Earth Environ. Sci. 27 (2015), 012068, https://doi.org/10.1088/1755-1315/27/1/012068.

[7] T. Kousksou, P. Bruel, A. Jamil, T. El Rhafiki, Y. Zeraouli, Energy Storage: Applications and Challenges, Solar Energy Materials and Solar Cells, vol. 120, 2014, pp. 59–80, https://doi.org/10.1016/j.solmat.2013.08.015.

[8] J.O. Abe, A.P.I. Popoola, E. Ajenifuja, O.M. Popoola, Hydrogen energy, economy and storage: review and recommendation, Int. J. Hydrogen Energy 44 (2019) 15072–15086, https://doi.org/10.1016/j.ijhydene.2019.04.068.

[9] J. Koponen, Review of Water Electrolysis Technologies and Design of Renewable Hydrogen Production Systems, 2015, p. 94.

[10] M. Carmo, D.L. Fritz, J. Mergel, D. Stolten, A comprehensive review on PEM water electrolysis, Int. J. Hydrogen Energy 38 (2013) 4901–4934, https://doi.org/10.1016/j.ijhydene.2013.01.151.

[11] E. Fabbri, T.J. Schmidt, Oxygen evolution reaction - the enigma in water electrolysis, ACS Catal. 8 (2018) 9765–9774, https://doi.org/10.1021/acscatal.8b02712.

[12] K. Kinoshita, Carbon: Electrochemical and Physicochemical Properties, New York: Wiley, 1988, 1988.

[13] P. Mazúr, J. Polonský, M. Paidar, K. Bouzek, Non-conductive TiO 2 as the anode catalyst support for PEM water electrolysis, Int. J. Hydrogen Energy 37 (2012) 12081–12088, https://doi.org/10.1016/j.ijhydene.2012.05.129.

[14] P. Kúš, Thin-Film Catalysts for Proton Exchange Membrane Water Electrolyzers and Unitized Regenerative Fuel Cells, Springer International Publishing, Cham, 2019, https://doi.org/10.1007/978-3-030-20859-2.

[15] G. Li, K. Li, L. Yang, J. Chang, R. Ma, Z. Wu, J. Ge, C. Liu, W. Xing, Boosted performance of Ir species by employing TiN as the support toward oxygen evolution reaction, ACS Appl. Mater. Interfaces 10 (2018) 38117–38124, https://doi.org/10.1021/acsami.8b14172.

[16] J. Polonský, P. Mazúr, M. Paidar, E. Christensen, K. Bouzek, Performance of a PEM water electrolyser using a TaC-supported iridium oxide electrocatalyst, Int. J. Hydrogen Energy 39 (2014) 3072–3078, https://doi.org/10.1016/j.ijhydene.2013.12.085.

[17] J. Xu, G. Liu, J. Li, X. Wang, The electrocatalytic properties of an IrO 2/SnO 2 catalyst using SnO 2 as a support and an assisting reagent for the oxygen evolution reaction, Electrochim. Acta 59 (2012) 105–112, https://doi.org/10.1016/j.electacta.2011.10.044.

[18] M. Bernt, A. Hartig-Weiß, M.F. Tovini, H.A. El-Sayed, C. Schramm, J. Schröter, C. Gebauer, H.A. Gasteiger, Current challenges in catalyst development for PEM water electrolyzers, Chem. Ing. Tech. 92 (2020) 31–39, https://doi.org/10.1002/cite.201900101.

[19] T. Hrbek, P. Kúš, Y. Yakovlev, J. Nováková, Y. Lobko, I. Khalakhan, V. Matolín, I. Matolínová, Sputter-etching treatment of proton-exchange membranes: completely dry thin-film approach to low-loading catalyst-coated membranes for water electrolysis, Int. J. Hydrogen Energy 45 (2020) 20776–20786, https://doi.org/10.1016/j.ijhydene.2020.05.245.

[20] J. Liang, Q. Liu, T. Li, Y. Luo, S. Lu, X. Shi, F. Zhang, A.M. Asiri, X. Sun, Magnetron sputtering enabled sustainable synthesis of nanomaterials for energy electrocatalysis, Green Chem. 23 (2021) 2834–2867, https://doi.org/10.1039/d0gc03994b.

[21] I. Khalakhan, M. Vorokhta, P. Kúš, M. Dopita, M. Václavů, R. Fiala, N. Tsud, T. Skála, V. Matolín, In situ probing of magnetron sputtered Pt-Ni alloy fuel cell catalysts during accelerated durability test using EC-AFM, Electrochim. Acta 245 (2017) 760–769, https://doi.org/10.1016/j.electacta.2017.05.202.

[22] I. Khalakhan, M. Dubau, S. Haviar, J. Lavková, I. Matolínová, V. Potin, M. Vorokhta, V. Matolín, Growth of nano-porous Pt-doped cerium oxide thin films on glassy carbon substrate, Ceram. Int. 39 (2013) 3765–3769, https://doi.org/10.1016/j.ceramint.2012.10.215.

[23] P. Kúš, A. Ostroverkh, I. Khalakhan, R. Fiala, Y. Kosto, B. Šmíd, Y. Lobko, Y. Yakovlev, J. Nováková, I. Matolínová, V. Matolín, Magnetron sputtered thin-film vertically segmented Pt-Ir catalyst supported on TiC for anode side of proton exchange membrane unitized regenerative fuel cells, Int. J. Hydrogen Energy 44 (2019) 16087–16098, https://doi.org/10.1016/j.ijhydene.2019.04.216.

[24] A. Ostroverkh, V. Johanek, M. Dubau, P. Kus, K. Veltruska, M. Vaclavu, R. Fiala, B. Smid, Y. Ostroverkh, V. Matolin, Novel fuel cell MEA based on Pt-C deposited by magnetron sputtering, ECS Trans. 80 (2017) 225–230, https://doi.org/10.1149/08008.0225ecst.

[25] H. Wei, H. Eilers, From silver nanoparticles to thin films: evolution of microstructure and electrical conduction on glass substrates, J. Phys. Chem. Solid. 70 (2009) 459–465, https://doi.org/10.1016/j.jpcs.2008.11.012.

[26] G. Bräuer, Magnetron Sputtering, Comprehensive Materials Processing, vol. 4, 2014, pp. 57–73, https://doi.org/10.1016/B978-0-08-096532-1.00403-9.

[27] M.S. Burke, L.J. Enman, A.S. Batchellor, S. Zou, S.W. Boettcher, Oxygen evolution reaction electrocatalysis on transition metal oxides and (Oxy)hydroxides: activity trends and design principles, Chem. Mater. 27 (2015) 7549–7558, https://doi.org/10.1021/acs.chemmater.5b03148.

[28] Y. Zhu, W. Zhou, Z. Shao, Perovskite/carbon composites: applications in oxygen electrocatalysis, Small 13 (2017), 1603793, https://doi.org/10.1002/smll.201603793.

[29] Y. Zhu, H.A. Tahini, Z. Hu, Y. Yin, Q. Lin, H. Sun, Y. Zhong, Y. Chen, F. Zhang, H. Lin, C. Chen, W. Zhou, X. Zhang, S.C. Smith, Z. Shao, H. Wang, Boosting oxygen evolution reaction by activation of lattice-oxygen sites in layered Ruddlesden-Popper oxide, EcoMat 2 (2020), https://doi.org/10.1002/eom2.12021.

[30] Y. Zhu, H.A. Tahini, Z. Hu, Z. Chen, W. Zhou, A.C. Komarek, Q. Lin, H. Lin, C. Chen, Y. Zhong, M.T. Fernández-Díaz, S.C. Smith, H. Wang, M. Liu, Z. Shao, Boosting oxygen evolution reaction by creating both metal ion and lattice-oxygen active sites in a complex oxide, Adv. Mater. 32 (2020), 1905025, https://doi.org/10.1002/adma.201905025.

[31] J. Yu, Q. He, G. Yang, W. Zhou, Z. Shao, M. Ni, Recent advances and prospective in ruthenium-based materials for electrochemical water splitting, ACS Catal. 9 (2019) 9973–10011, https://doi.org/10.1021/acscatal.9b02457.

[32] R. Kötz, S. Stucki, Stabilization of RuO2 by IrO2 for anodic oxygen evolution in acid media, Electrochim. Acta 31 (1986) 1311–1316, https://doi.org/10.1016/0013-4686(86)80153-0.

[33] V.A. Saveleva, L. Wang, W. Luo, S. Zafeiratos, C. Ulhaq-Bouillet, A.S. Gago, K. A. Friedrich, E.R. Savinova, Uncovering the stabilization mechanism in bimetallic ruthenium-iridium anodes for proton exchange membrane electrolyzers, J. Phys. Chem. Lett. 7 (2016) 3240–3245, https://doi.org/10.1021/acs.jpclett.6b01500.

[34] S. Cherevko, S. Geiger, O. Kasian, N. Kulyk, J.P. Grote, A. Savan, B.R. Shrestha, S. Merzlikin, B. Breitbach, A. Ludwig, K.J.J. Mayrhofer, Oxygen and hydrogen evolution reactions on Ru, RuO2, Ir, and IrO2 thin film electrodes in acidic and alkaline electrolytes: a comparative study on activity and stability, Catal. Today 262 (2016) 170–180, https://doi.org/10.1016/j.cattod.2015.08.014.

[35] D. Escalera-López, S. Czioska, J. Geppert, A. Boubnov, P. Röse, E. Saraçi, U. Krewer, J.D. Grunwaldt, S. Cherevko, Phase- and surface composition-dependent electrochemical stability of Ir-Ru nanoparticles during oxygen evolution reaction, ACS Catal. 11 (2021) 9300–9316, https://doi.org/10.1021/acscatal.1c01682.

[36] I.M. Tomáš Hrbek, Peter Kúš, Tereza Košutová, Kateřina Veltruská, Thu Ngan Dinhová, Milan Dopita, Vladimír Matolín, Sputtered Ir-Ru based catalysts for oxygen evolution reaction: Study of iridium effect on stability, International Journal of Hydrogen Energy (In PRESS). (n.d.).

[37] D. Siegmund, S. Metz, V. Peinecke, T.E. Warner, C. Cremers, A. Grevé, T. Smolinka, D. Segets, U. Apfel, crossing the valley of death: from fundamental to applied research in electrolysis, JACS Au 1 (2021) 527–535, https://doi.org/10.1021/jacsau.1c00092.

[38] J. Knöppel, M. Möckl, D. Escalera-López, K. Stojanovski, M. Bierling, T. Böhm, S. Thiele, M. Rzepka, S. Cherevko, On the limitations in assessing stability of oxygen evolution catalysts using aqueous model electrochemical cells, Nat. Commun. 12 (2021), https://doi.org/10.1038/s41467-021-22296-9.

[39] K. Ehelebe, D. Escalera-López, S. Cherevko, Limitations of aqueous model systems in the stability assessment of electrocatalysts for oxygen reactions in fuel cell and electrolyzers, Curr Opin Electrochem 29 (2021), https://doi.org/10.1016/j.coelec.2021.100832.

[40] V. Saveleva, Investigation of the Anodes of PEM Water Electrolyzers by Operando Synchrotron-Based Photoemission Spectroscopy, 2018, p. 296.

[41] M.E. Orazem, B. Tribollet, Electrochemical Impedance Spectroscopy, John Wiley & Sons, Inc., Hoboken, NJ, USA, 2008, https://doi.org/10.1002/9780470381588.

[42] A.M. Dhirde, N.V. Dale, H. Salehfar, M.D. Mann, T.H. Han, Equivalent electric circuit modeling and performance analysis of a PEM fuel cell stack using impedance spectroscopy, IEEE Trans. Energy Convers. 25 (2010) 778–786, https://doi.org/10.1109/TEC.2010.2049267.

[43] S. Siracusano, S. Trocino, N. Briguglio, V. Baglio, A.S. Aricò, Electrochemical impedance spectroscopy as a diagnostic tool in polymer electrolyte membrane electrolysis, Materials 11 (2018), https://doi.org/10.3390/ma11081368.

[44] P. Kúš, A. Ostroverkh, K. Ševčíková, I. Khalakhan, R. Fiala, T. Skála, N. Tsud, V. Matolin, Magnetron sputtered Ir thin film on TiC-based support sublayer as low-loading anode catalyst for proton exchange membrane water electrolysis, Int. J. Hydrogen Energy 41 (2016) 15124–15132, https://doi.org/10.1016/j.ijhydene.2016.06.248.

[45] Bruker-Nano, Introduction to EDS Analysis - Reference Manual, 2011, 0–53.

[46] J. Végh, The Shirley background revised, J. Electron. Spectrosc. Relat. Phenom. 151 (2006) 159–164, https://doi.org/10.1016/j.elspec.2005.12.002.

[47] V. Jain, M.C. Biesinger, M.R. Linford, The Gaussian-Lorentzian Sum, Product, and Convolution (Voigt) functions in the context of peak fitting X-ray photoelectron spectroscopy (XPS) narrow scans, Appl. Surf. Sci. 447 (2018) 548–553, https://doi.org/10.1016/j.apsusc.2018.03.190.

[48] D. Shah, V. Fernandez, M.R. Linford, Advanced Line Shapes in, 2020.

[49] G.H. Major, N. Fairley, P.M.A. Sherwood, M.R. Linford, J. Terry, V. Fernandez, K. Artyushkova, Practical guide for curve fitting in x-ray photoelectron spectroscopy, J. Vac. Sci. Technol. 38 (2020), 061203, https://doi.org/10.1116/6.0000377.

[50] A.G. Shard, J.D.P. Counsell, D.J.H. Cant, E.F. Smith, P. Navabpour, X. Zhang, C. J. Blomfield, Intensity calibration and sensitivity factors for XPS instruments with

monochromatic Ag Lα and Al Kα sources, Surf. Interface Anal. 51 (2019) 763–773, https://doi.org/10.1002/sia.6647.
[51] V.K. Puthiyapura, S. Pasupathi, H. Su, X. Liu, B. Pollet, K. Scott, Investigation of supported IrO2 as electrocatalyst for the oxygen evolution reaction in proton exchange membrane water electrolyser, Int. J. Hydrogen Energy 39 (2014) 1905–1913, https://doi.org/10.1016/j.ijhydene.2013.11.056.
[52] M. Bernt, A. Siebel, H.A. Gasteiger, Analysis of voltage losses in PEM water electrolyzers with low platinum group metal loadings, J. Electrochem. Soc. 165 (2018), https://doi.org/10.1149/2.0641805jes. F305–F314.
[53] S. Song, H. Zhang, X. Ma, Z. Shao, R.T. Baker, B. Yi, Electrochemical investigation of electrocatalysts for the oxygen evolution reaction in PEM water electrolyzers, Int. J. Hydrogen Energy 33 (2008) 4955–4961, https://doi.org/10.1016/j.ijhydene.2008.06.039.
[54] J. Lim, G. Kang, J.W. Lee, S.S. Jeon, H. Jeon, P.W. Kang, H. Lee, Amorphous Ir atomic clusters anchored on crystalline IrO2 nanoneedles for proton exchange membrane water oxidation, J. Power Sources 524 (2022), 231069, https://doi.org/10.1016/j.jpowsour.2022.231069.
[55] F. Hegge, F. Lombeck, E. Cruz Ortiz, L. Bohn, M. Von Holst, M. Kroschel, J. Hübner, M. Breitwieser, P. Strasser, S. Vierrath, Efficient and stable low iridium loaded anodes for PEM water electrolysis made possible by nanofiber interlayers, ACS Appl. Energy Mater. 3 (2020) 8276–8284, https://doi.org/10.1021/acsaem.0c00735.
[56] C. Rozain, E. Mayousse, N. Guillet, P. Millet, Influence of iridium oxide loadings on the performance of PEM water electrolysis cells: Part II - advanced oxygen electrodes, Appl. Catal., B 182 (2016) 123–131, https://doi.org/10.1016/j.apcatb.2015.09.011.
[57] L. Wang, V.A. Saveleva, S. Zafeiratos, E.R. Savinova, P. Lettenmeier, P. Gazdzicki, A.S. Gago, K.A. Friedrich, Highly active anode electrocatalysts derived from electrochemical leaching of Ru from metallic Ir0.7Ru0.3 for proton exchange membrane electrolyzers, Nano Energy 34 (2017) 385–391, https://doi.org/10.1016/j.nanoen.2017.02.045.
[58] S. Shiva Kumar, V. Himabindu, Hydrogen production by PEM water electrolysis – a review, Mater Sci Energy Technol 2 (2019) 442–454, https://doi.org/10.1016/j.mset.2019.03.002.
[59] G. Papakonstantinou, G. Algara-Siller, D. Teschner, T. Vidaković-Koch, R. Schlögl, K. Sundmacher, Degradation study of a proton exchange membrane water electrolyzer under dynamic operation conditions, Appl. Energy 280 (2020), https://doi.org/10.1016/j.apenergy.2020.115911.
[60] P. Petzoldt, J.T.H. Kwan, A. Bonakdarpour, D. Wilkinson, Deconvoluting reversible and irreversible degradation phenomena in OER catalyst coated membranes using a modified RDE technique, J. Electrochem. Soc. (2021), https://doi.org/10.1149/1945-7111/abde7d.
[61] J.H. Kim, C.Y. Oh, K.R. Kim, J.P. Lee, T.J. Kim, Electrical double layer mechanism analysis of PEM water electrolysis for frequency limitation of pulsed currents, Energies 14 (2021), https://doi.org/10.3390/en14227822.
[62] P. Gazdzick, J. Mitzel, D. Garcia Sanchez, M. Schulze, K.A. Friedrich, Evaluation of reversible and irreversible degradation rates of polymer electrolyte membrane fuel cells tested in automotive conditions, J. Power Sources 327 (2016) 86–95, https://doi.org/10.1016/j.jpowsour.2016.07.049.
[63] H. Yu, L. Bonville, J. Jankovic, R. Maric, Microscopic insights on the degradation of a PEM water electrolyzer with ultra-low catalyst loading, Appl. Catal., B 260 (2020), 118194, https://doi.org/10.1016/j.apcatb.2019.118194.
[64] S. Siracusano, N. Van Dijk, R. Backhouse, L. Merlo, V. Baglio, A.S. Aricò, Degradation issues of PEM electrolysis MEAs, Renew. Energy 123 (2018) 52–57, https://doi.org/10.1016/j.renene.2018.02.024.
[65] S. Zhao, A. Stocks, B. Rasimick, K. More, H. Xu, Highly active, durable dispersed iridium nanocatalysts for PEM water electrolyzers, J. Electrochem. Soc. 165 (2018) F82–F89, https://doi.org/10.1149/2.0981802jes.
[66] S. Siracusano, V. Baglio, S.A. Grigoriev, L. Merlo, V.N. Fateev, A.S. Aricò, The influence of iridium chemical oxidation state on the performance and durability of oxygen evolution catalysts in PEM electrolysis, J. Power Sources 366 (2017) 105–114, https://doi.org/10.1016/j.jpowsour.2017.09.020.
[67] D. Kulkarni, A. Huynh, P. Satjaritanun, M. O'Brien, S. Shimpalee, D. Parkinson, P. Shevchenko, F. DeCarlo, N. Danilovic, K.E. Ayers, C. Capuano, I.V. Zenyuk, Elucidating effects of catalyst loadings and porous transport layer morphologies on operation of proton exchange membrane water electrolyzers, Appl. Catal., B 308 (2022), 121213, https://doi.org/10.1016/j.apcatb.2022.121213.
[68] A. Lim, J. Kim, H.J. Lee, H.J. Kim, S.J. Yoo, J.H. Jang, H. Young Park, Y.E. Sung, H.S. Park, Low-loading IrO2 supported on Pt for catalysis of PEM water electrolysis and regenerative fuel cells, Appl. Catal., B 272 (2020), 118955, https://doi.org/10.1016/j.apcatb.2020.118955.
[69] J. Ni, Z. Shi, X. Wang, Y. Wang, H. Wu, C. Liu, J. Ge, W. Xing, Recent Development of Low Iridium Electrocatalysts towards Efficient Water Oxidation, 2022, https://doi.org/10.13208/j.electrochem.
[70] P.T. Kissinger, W.R. Heineman, Cyclic voltammetry, J Chem Educ 60 (1983) 702–706, https://doi.org/10.1021/ed060p702.
[71] S. Kocha, I. Consultant, Artifacts in Measuring Electrode Catalyst Area of Fuel Cells through Cyclic Voltammetry, 2016, https://doi.org/10.1149/1.2780954.
[72] M. Pourbaix, H. Zhang, A. Pourbaix, Presentation of an Atlas of chemical and electrochemical equilibria in the presence of a gaseous phase, Mater. Sci. Forum 251–254 (1997) 143–148. https://doi.org/10.4028/www.scientific.net/msf.251-254.143.
[73] J. van der Merwe, K. Uren, G. van Schoor, D. Bessarabov, Characterisation tools development for PEM electrolysers, Int. J. Hydrogen Energy 39 (2014) 14212–14221, https://doi.org/10.1016/j.ijhydene.2014.02.096.
[74] M. Chandesris, V. Médeau, N. Guillet, S. Chelghoum, D. Thoby, F. Fouda-Onana, Membrane degradation in PEM water electrolyzer: numerical modeling and experimental evidence of the influence of temperature and current density, Int. J. Hydrogen Energy 40 (2015) 1353–1366, https://doi.org/10.1016/j.ijhydene.2014.11.111.
[75] M. Suermann, T.J. Schmidt, F.N. Büchi, Investigation of mass transport losses in polymer electrolyte electrolysis cells, ECS Meeting Abstracts MA2015–02 (2015), https://doi.org/10.1149/ma2015-02/37/1517, 1517–1517.
[76] K. Park, B.Y. Chang, S. Hwang, Correlation between Tafel analysis and electrochemical impedance spectroscopy by prediction of amperometric response from EIS, ACS Omega 4 (2019) 19307–19313, https://doi.org/10.1021/acsomega.9b02672.
[77] H. Vrubel, T. Moehl, M. Grätzel, X. Hu, Revealing and accelerating slow electron transport in amorphous molybdenum sulphide particles for hydrogen evolution reaction, Chem. Commun. 49 (2013) 8985–8987, https://doi.org/10.1039/c3cc45416a.
[78] C.G. Morales-Guio, L. Liardet, X. Hu, Oxidatively electrodeposited thin-film transition metal (Oxy)hydroxides as oxygen evolution catalysts, J. Am. Chem. Soc. 138 (2016) 8946–8957, https://doi.org/10.1021/jacs.6b05196.
[79] O.E. Meiron, V. Kuraganti, I. Hod, R. Bar-Ziv, M. Bar-Sadan, Improved catalytic activity of Mo1-: XWxSe2 alloy nanoflowers promotes efficient hydrogen evolution reaction in both acidic and alkaline aqueous solutions, Nanoscale 9 (2017) 13998–14005, https://doi.org/10.1039/c7nr04922f.
[80] M. Suermann, B. Bensmann, R. Hanke-Rauschenbach, Degradation of proton exchange membrane (PEM) water electrolysis cells: looking beyond the cell voltage increase, J. Electrochem. Soc. 166 (2019) F645–F652, https://doi.org/10.1149/2.1451910jes.
[81] C. Gerling, M. Hanauer, U. Berner, K. Andreas Friedrich, PEM single cells under differential conditions: full factorial parameterization of the ORR and HOR kinetics and loss analysis, J. Electrochem. Soc. 169 (2022), 014503, https://doi.org/10.1149/1945-7111/ac44ba.
[82] T. Audichon, T.W. Napporn, C. Canaff, C. Morais, C. Comminges, K.B. Kokoh, IrO2 coated on RuO2 as efficient and stable electroactive nanocatalysts for electrochemical water splitting, J. Phys. Chem. C 120 (2016) 2562–2573, https://doi.org/10.1021/acs.jpcc.5b11868.
[83] E. Antolini, Iridium as catalyst and cocatalyst for oxygen evolution/reduction in acidic polymer electrolyte membrane electrolyzers and fuel cells, ACS Catal. 4 (2014) 1426–1440, https://doi.org/10.1021/cs4011875.
[84] A. Sharma, F.J. Beck, Quantifying and comparing fundamental loss mechanisms to enable solar-to-hydrogen conversion efficiencies above 20% using perovskite-silicon tandem absorbers, Advanced Energy and Sustainability Research 2 (2021), 2000039, https://doi.org/10.1002/aesr.202000039.
[85] E. Cuervo-Reyes, C.P. Scheller, M. Held, U. Sennhauser, A unifying view of the constant-phase-element and its role as an aging indicator for Li-ion batteries, J. Electrochem. Soc. 162 (2015), https://doi.org/10.1149/2.0791508jes. A1585–A1591.
[86] Z. Lukács, T. Kristóf, A generalized model of the equivalent circuits in the electrochemical impedance spectroscopy, Electrochim. Acta 363 (2020), 137199, https://doi.org/10.1016/j.electacta.2020.137199.
[87] S. Holm, Time domain characterization of the Cole-Cole dielectric model, J Electr Bioimpedance 11 (2020) 101–105, https://doi.org/10.2478/JOEB-2020-0015.
[88] P. Córdoba-Torres, T.J. Mesquita, O. Devos, B. Tribollet, V. Roche, R.P. Nogueira, On the intrinsic coupling between constant-phase element parameters α and Q in electrochemical impedance spectroscopy, Electrochim. Acta 72 (2012) 172–178, https://doi.org/10.1016/j.electacta.2012.04.020.
[89] C.H. Hsu, F. Mansfeld, Concernng the conversion of the constant phase element parameter Y0 into a capacitance, Corrosion 57 (2001) 747–748, https://doi.org/10.5006/1.3280607.
[90] A.J. Bard, L.R. Faulkner, Electrochemical Methods Fundamentals and Applications, 2001.
[91] J.P. Sabawa, A.S. Bandarenka, Applicability of double layer capacitance measurements to monitor local temperature changes at polymer electrolyte membrane fuel cell cathodes, Results Chem 2 (2020), 100078, https://doi.org/10.1016/j.rechem.2020.100078.
[92] B.B. Berkes, J.B. Henry, M. Huang, A.S. Bondarenko, Electrochemical characterisation of copper thin-film formation on polycrystalline platinum, ChemPhysChem 13 (2012) 3210–3217, https://doi.org/10.1002/cphc.201200193.
[93] J. Kwen, G. Doo, S. Choi, H. Guim, S. Yuk, D.H. Lee, D.W. Lee, J. Hyun, H.T. Kim, Identification of the electrical connection in the catalyst layer of the polymer electrolyte membrane water electrolyzer, Int. J. Hydrogen Energy (2022), https://doi.org/10.1016/j.ijhydene.2022.02.136.
[94] H. Guo, H. Li, D. Fernandez, S. Willis, K. Jarvis, G. Henkelman, S.M. Humphrey, Stabilizer-free CuIr alloy nanoparticle catalysts, Chem. Mater. 31 (2019) 10225–10235, https://doi.org/10.1021/acs.chemmater.9b04138.
[95] V. Pfeifer, T.E. Jones, J.J. Velasco Vélez, C. Massué, R. Arrigo, D. Teschner, F. Girgsdies, M. Scherzer, M.T. Greiner, J. Allan, M. Hashagen, G. Weinberg, S. Piccinin, M. Hävecker, A. Knop-Gericke, R. Schlögl, The electronic structure of iridium and its oxides, Surf. Interface Anal. 48 (2016) 261–273, https://doi.org/10.1002/sia.5895.
[96] S.J. Freakley, J. Ruiz-Esquius, D.J. Morgan, The X-ray photoelectron spectra of Ir, IrO2 and IrCl3 revisited, Surf. Interface Anal. 49 (2017) 794–799, https://doi.org/10.1002/sia.6225.
[97] Z. Novotny, B. Tobler, L. Artiglia, M. Fischer, M. Schreck, J. Raabe, J. Osterwalder, Kinetics of the thermal oxidation of Ir(100) toward IrO2 studied

by ambient-pressure X-ray photoelectron spectroscopy, J. Phys. Chem. Lett. 11 (2020) 3601–3607, https://doi.org/10.1021/acs.jpclett.0c00914.
[98] S. Czioska, A. Boubnov, D. Escalera-López, J. Geppert, A. Zagalskaya, P. Röse, E. Saraçi, V. Alexandrov, U. Krewer, S. Cherevko, J.D. Grunwaldt, Increased Ir-Ir interaction in iridium oxide during the oxygen evolution reaction at high potentials probed by operando spectroscopy, ACS Catal. 11 (2021) 10043–10057, https://doi.org/10.1021/acscatal.1c02074.
[99] D.J. Morgan, Resolving ruthenium: XPS studies of common ruthenium materials, Surf. Interface Anal. 47 (2015) 1072–1079, https://doi.org/10.1002/sia.5852.
[100] S. Takabayashi, K. Okamoto, T. Nakatani, H. Sakaue, T. Takahagi, Surface analysis of carbon-hydrogen bonds in diamondlike carbon films by X-ray photoelectron spectroscopy, Jpn. J. Appl. Phys. 48 (2009) 923041–923045, https://doi.org/10.1143/JJAP.48.092304.
[101] A.K. Friedman, W. Shi, Y. Losovyj, A.R. Siedle, L.A. Baker, Mapping microscale chemical heterogeneity in nafion membranes with X-ray photoelectron spectroscopy, J. Electrochem. Soc. 165 (2018) H733–H741, https://doi.org/10.1149/2.0771811jes.